JOURNAL OF SPACECRAFT AND ROCKETS
Vol. 29, No. 5, September-October 1992

Viscous Equilibrium Computations Using Program LAURA

Francis A. Greene* and Roop N. Gupta†
NASA Langley Research Center, Hampton, Virginia 23665

Modifications have been made to the Langley Aerothermodynamic Upwind Relaxation Algorithm (LAURA) that enable it to compute viscous airflows under the assumption of thermal and chemical equilibrium. Equilibrium thermodynamic and transport property information are input to the code via curve fits. The periodic updating of this information enables the equilibrium algorithm to perform at a computational rate that is only a small percentage larger than the rate associated with the perfect-gas algorithm. Presented in this article are the results of the initial validation of the modified code. Solutions for surface pressure and heating are presented for the flow over slender and blunt cones at realistic re-entry conditions. LAURA solutions are compared with those produced by a viscous shock-layer method, and, for one case considered, with heat transfer data from a flight experiment. For both pressure and heating, the agreement is good. In general, differences in pressures of a few percent were noted, while differences in heating rates were in the 5-10% range.

Nomenclature

A = Jacobian matrix of g with respect to q
B = Jacobian matrix of h with respect to q
E = total energy per unit mass, J/kg
e = internal energy per unit mass, J/kg
g = inviscid flux vector
H = total enthalpy per unit mass, J/kg
h = enthalpy per unit mass, J/kg
h = viscous flux vector
I = identity matrix
M = right eigenvector matrix of A
M^{-1} = left eigenvector matrix of A
n = outward unit normal vector of a cell face
Pr = total Prandtl number
p = pressure, N/m^2
Re = freestream Reynolds number
Rn = nose radius, m
S = arc length distance along symmetry plane, m
t = time, s
U = contravariant velocity normal to a cell face
u = velocity component in x direction, m/s
V = velocity vector, m/s
v = velocity component in y direction, m/s
w = velocity component in z direction, m/s
γ = h/e
λ = eigenvalue matrix of A
μ = viscosity, N-s/m^2
ρ = density, kg/m^3
σ = cell face area, m^2
Ω = cell volume, m^3

Introduction

THE LAURA computer program, as initially developed by Gnoffo,[1-3] was a three-dimensional finite-volume thin-layer Navier-Stokes solver for computing perfect-gas blunt-body and wake flows. Gnoffo has subsequently extended LAURA to compute flows in thermal and chemical nonequilibrium.[4] Since its inception, the perfect-gas algorithm has been modified and used to analyze specific problems. Some of the problems that have been examined include heating on slender vehicles,[5] winged vehicle aerodynamics,[6,7] and thermochemical issues associated with Earth re-entry from Mars.[8] The successful application of the LAURA code to blunt, slender, and winged vehicles, and its use over a wide hypersonic Mach number range, demonstrates the robust nature of the algorithm.

Various concepts for hypersonic vehicles are currently being studied. Vehicles ranging from those designed for a ballistic entry and parachute landing to aerodynamically complex winged shapes designed for vertical take off and conventional landings are under consideration for hypersonic flight applications. Upon Earth re-entry, the temperatures within the shock layer surrounding these hypersonic vehicles are sufficient to initiate chemical reactions. Conventional ground-based test facilities are unable to reproduce these high-temperature effects at desired flight conditions, and, therefore, can offer no information on how a chemically reacting shock layer may influence the aerothermodynamic aspects of a vehicle. Other than flight experiments, which can be years in the making, computational methods offer the only avenue to determine aerothermodynamic information within a chemically reacting shock layer associated with hypersonic flight conditions.

The LAURA algorithm described in Ref. 4 is capable of predicting airflows that are near chemical and thermal equilibrium. However, its performance is considerably slower than that of the perfect-gas algorithm. For equilibrium airflows in which gross information about the aerothermodynamics is desired and detailed flowfield information associated with the aerothermochemistry is not necessary, more cost effective approaches of obtaining gross flowfield and surface solutions are available. The focus of this work was to develop a tool that performs at a computational rate comparable with that of the perfect-gas algorithm and is able to predict the viscous equilibrium air flowfield surrounding a vehicle traveling at a hypersonic velocity. To accomplish this objective, the inviscid LAURA algorithm described in Ref. 7 is used as a starting point, and the thin-layer Navier-Stokes terms and curve fits for both Prandtl number Pr and viscosity μ were added to it.

To validate the viscous equilibrium air option, LAURA predictions for surface pressure and surface heating are compared with corresponding predictions from a viscous-shock-layer (VSL) technique[9] and, in one case, with heating data from a flight experiment.[10] Cone solutions for three flow conditions are presented. Comparisons are made for a Mach

Received Oct. 27, 1991; revision received April 13, 1992; accepted for publication April 13, 1992.

*Aerospace Engineer, Aerothermodynamics Branch, Space Systems Division. Member AIAA.

†Aerospace Engineer, Aerothermodynamics Branch, Space Systems Division. Associate Fellow AIAA.

19 flow at 36-km altitude, a Mach 25 flow at 60-km altitude, and a Mach 40 flow at 70-km altitude. For the three cases, the angle of attack is 0 deg and an axisymmetric flow is assumed.

Governing Equations

The inviscid LAURA algorithm with equilibrium-air and tetrafluoromethane (CF_4) options, described in Ref. 7, was extended to include the effects of viscosity. The viscous predictions are based on the thin-layer Navier-Stokes equations, with the shear stress and heat flux terms incorporated as documented in Ref. 3. The following paragraphs give an overview of the formulation of the governing equations, including the modifications which enable viscous equilibrium airflows to be computed.

Following the form given in Ref. 3, the integral form of the governing equations is

$$\iiint q_t \, d\Omega + \iint (f \cdot n) \, d\sigma = 0 \tag{1}$$

where q_t represents the time rate of change of the dependent variable vector q, and f represents the sum of the inviscid and viscous flux. The vectors f and q are

$$f = \begin{bmatrix} \rho u \\ \rho uu + p - \tau_{xx} \\ \rho uv - \tau_{xy} \\ \rho uw - \tau_{xz} \\ \rho uH - \dot{q}_x - V \cdot \tau_x \end{bmatrix} i + \begin{bmatrix} \rho v \\ \rho vu - \tau_{yx} \\ \rho vv + p - \tau_{yy} \\ \rho vw - \tau_{yz} \\ \rho vH - \dot{q}_y - V \cdot \tau_y \end{bmatrix} j + \begin{bmatrix} \rho w \\ \rho wu - \tau_{zx} \\ \rho wv - \tau_{zy} \\ \rho ww + p - \tau_{zz} \\ \rho wH - \dot{q}_z - V \cdot \tau_z \end{bmatrix} k, \qquad q = \begin{bmatrix} \rho \\ \rho u \\ \rho v \\ \rho w \\ \rho E \end{bmatrix}$$

where τ and $\dot{q}$ represent their indicated components of the stress tensor and the heat flux, respectively.

Expressing Eq. (1) in finite volume form for a single six-sided cell in the computational domain gives

$$\begin{aligned} \delta q_{i,j,k} = &- \left[\frac{\delta t}{\Omega}\right]_{i,j,k} [f_{i+\frac{1}{2}} \cdot n_{i+\frac{1}{2}} \sigma_{i+\frac{1}{2}} - f_{i-\frac{1}{2}} \cdot n_{i-\frac{1}{2}} \sigma_{i-\frac{1}{2}}]_{j,k} \\ &+ [f_{j+\frac{1}{2}} \cdot n_{j+\frac{1}{2}} \sigma_{j+\frac{1}{2}} - f_{j-\frac{1}{2}} \cdot n_{j-\frac{1}{2}} \sigma_{j-\frac{1}{2}}]_{i,k} \\ &+ [f_{k+\frac{1}{2}} \cdot n_{k+\frac{1}{2}} \sigma_{k+\frac{1}{2}} - f_{k-\frac{1}{2}} \cdot n_{k-\frac{1}{2}} \sigma_{k-\frac{1}{2}}]_{i,j} \end{aligned} \tag{2}$$

where $\delta(\ )$ represents a time change in the quantity $(\ )$. The lower case subscripts indicate values at the cell center, unless offset by a half, in which case they indicate values at the center of a cell face. A shorthand notation that will be used in this paper enables Eq. (2) to be written as

$$\delta q_{i,j,k} = \left[\frac{\delta t}{\Omega}\right]_{i,j,k} \sum_{l=i,j,k} \{[(g + h) \cdot n\sigma]_{l-\frac{1}{2}} - [(g + h) \cdot n\sigma]_{l+\frac{1}{2}}\} \tag{3}$$

where g and h are the inviscid and viscous portions of f, respectively.

The first-order inviscid flux at the center of a cell face is computed using Roe's scheme,[11] and second-order fluxes are computed using Yee's symmetric total variation diminishing (STVD) approach.[12] Neglecting the vector symbol, the inviscid flux is defined as

$$g_{l+\frac{1}{2}} = \tfrac{1}{2}[g(q_l) + g(q_{l+1}) - [M|\lambda|(d - d^{\min})]_{l+\frac{1}{2}}] \tag{4}$$

where

$$d_{l+\frac{1}{2}} = M^{-1}_{l+\frac{1}{2}} \Delta q_{l+\frac{1}{2}} \tag{5}$$

and $\Delta(\ )$ represents a spatial change in the quantity $(\ )$. The right (M) and left (M^{-1}) eigenvector matrices and the eigenvalue (λ) matrix are given in Ref. 7. The elements of λ are subject to the eigenvalue limiter described in Ref. 3. For slender bodies, the limiter is used only when computing fluxes in the streamwise direction, but for blunt bodies it is used in all coordinate directions. Based on material presented in Ref. 3, the constant associated with the eigenvalue limiter was 0.05 and 0.20 for the slender and blunt bodies, respectively.

For second-order solutions, the STVD approach is used. This approach creates a second-order flux by applying a correction to the first-order dissipation term making it second-order accurate. This correction is performed using a min-mod function. This function compares values and is the smallest in absolute magnitude if the signs are the same, or is zero if the signs are different. Gradients of characteristic variables [Eq. (5)] are input to the min mod function. The min mod portion of the second-order term is

$$d^{\min} = \min \text{ mod}[d_1, d_2, d_3] \tag{6}$$

where the subscript 2 refers to the face at which the flux is being computed, 1 the face behind, and 3 the face ahead.

Second-order central differences are used to approximate the viscous stress and heat flux. The vector h under the thin-layer assumption is

$$h = \begin{bmatrix} 0 \\ -\tau_{nx} \\ -\tau_{ny} \\ -\tau_{nz} \\ -u\tau_{nx} - v\tau_{ny} - w\tau_{nz} - \dot{q}_n \end{bmatrix} \tag{7}$$

where

$$\tau_{ns} = \left[\frac{\mu}{Re}\right]\left[\frac{\partial v}{\partial \chi} + \frac{1}{3}\frac{\partial U}{\partial \chi} n_s\right][\nabla \chi \cdot n] \tag{8}$$

and

$$\dot{q}_n = \left[\frac{\mu}{RePr}\right]\left[\frac{\partial h}{\partial \chi} \nabla \chi \cdot n\right] \tag{9}$$

Provisions in the code allow these thin-layer terms to be included in any of the computational directions ($\chi = \xi$, η, or ζ). The variable s represents a Cartesian coordinate ($s = x, y, z$), and v the corresponding Cartesian velocity ($v = u, v, w$). Currently these terms are included only in the direction normal to the body ($\chi = \zeta$).

The discrete pressure jump across a cell face

$$\Delta p = \frac{\partial p}{\partial \rho}\Big|_{\rho e} \Delta \rho + \frac{\partial p}{\partial \rho e}\Big|_{\rho} \Delta(\rho e) \tag{10}$$

for a perfect-gas flow inherently satisfies Roe's property U.[11] However, this property is not inherently satisfied for equilibrium flow, since the ratio of specific heats is no longer constant. To address this, a technique attributed to Grossman[13] was incorporated in LAURA. This method does not satisfy identically the discrete pressure jump across a cell face, but approximates it based on theoretical considerations. The approximations are based on the work of Colella and Glaz.[14] With Grossman's formulation, the Roe's averaged variables retain their perfect-gas form. Further details can be found in Refs. 13 and 14.

For an equilibrium flow, with the heat flux expressed in terms of the gradient of enthalpy, where the enthalpy per unit mass h is

$$h = \left[\frac{p(\rho,e)}{\rho e} + 1\right] e = \gamma e \tag{11}$$

the Prandtl number in Eq. (9) is the total (equilibrium) Prandtl number. This Prandtl number is obtained from curve fits[15] and is based on values of total specific heat at constant pressure and total thermal conductivity. The total indicates that both frozen and reactive contributions are accounted for in the value. This formulation for obtaining surface heating is applicable when the heat flux is computed in a direction in which the pressure gradient is zero.[16] It is emphasized that γ in this formulation is not the ratio of the specific heats, but is an "effective" value which allows the perfect-gas equation of state to be used to recover the equilibrium pressure.

The viscous Jacobian $\boldsymbol{B}$ is shown below.

$$\boldsymbol{B} = \frac{\partial \boldsymbol{h}}{\partial q} + \frac{\partial \boldsymbol{h}}{\partial \gamma(\rho,e)} \frac{\partial \gamma(\rho,e)}{\partial q} \tag{12}$$

The first term in Eq. (12) is the perfect-gas viscous Jacobian given in Ref. 3. The second term, shown below, takes the variable γ into account.

$$\frac{\partial \boldsymbol{h}}{\partial \gamma(\rho,e)} \frac{\partial \gamma(\rho,e)}{\partial q} = \frac{\partial \boldsymbol{h}}{\partial \gamma} \left[\frac{\partial \gamma}{\partial \rho}\Big|_e \frac{\partial \rho}{\partial q} + \frac{\partial \gamma}{\partial e}\Big|_\rho \frac{\partial e}{\partial q} \right] = \frac{\mu e \nabla \chi \cdot \boldsymbol{n}}{RePr} \tag{13}$$

$$\times \begin{bmatrix} 0 & 0 & 0 & 0 & 0 \\ 0 & 0 & 0 & 0 & 0 \\ 0 & 0 & 0 & 0 & 0 \\ 0 & 0 & 0 & 0 & 0 \\ -[(\gamma_e/\rho)\omega + \gamma_\rho] & u\gamma_e/\rho & v\gamma_e/\rho & w\gamma_e/\rho & -\gamma_e/\rho \end{bmatrix} \tag{14}$$

The value of ω is defined as

$$\omega = 2[\boldsymbol{V} \cdot \boldsymbol{V}] - E \tag{15}$$

and the partials of γ are computed numerically from curve fit values of γ.

Accounting for both inviscid and viscous terms, the implicit form of the governing equations is

$$\left[I + \frac{\delta t}{\Omega} \boldsymbol{C} \right]_{i,j,k} \delta \boldsymbol{q}_{i,j,k} = \boldsymbol{r}_{i,j,k} \tag{16}$$

where

$$\boldsymbol{C}_{i,j,k} = \sum_{l=i,j,k} \{ [\tfrac{1}{2}|\boldsymbol{A}| + |\boldsymbol{B}|]_{l+\frac{1}{2}\sigma_{l+\frac{1}{2}}} + [\tfrac{1}{2}|\boldsymbol{A}| + |\boldsymbol{B}|]_{l-\frac{1}{2}\sigma_{l-\frac{1}{2}}} \} \tag{17}$$

and

$$\boldsymbol{r}_{i,j,k} = \left[\frac{\delta t}{\Omega} \right]_{i,j,k} \sum_{l=i,j,k} \{ [(\boldsymbol{g} + \boldsymbol{h}) \cdot \boldsymbol{n}\sigma]_{l-\frac{1}{2}} - [(\boldsymbol{g} + \boldsymbol{h}) \cdot \boldsymbol{n}\sigma]_{l+\frac{1}{2}} \} \tag{18}$$

Specific details of this formulation can be found in Ref. 3.

Equilibrium Model

To "close" the system of governing equations for an equilibrium airflow, relations between the thermodynamic variables along with expressions for the transport properties are required. These relations are in the form of curve fits. The thermodynamic curve fits used in the equilibrium version of LAURA were developed by Srinivasan et al.[17] They give pressure, temperature, and sound speed as a function of density and internal energy per unit mass. Srinivasan et al.'s curve fits are valid for temperatures up to 25,000 K and densities between 10^{-7} and 10^{3} amagats.

The transport property curve fits developed by Gupta et al.[15] give viscosity μ and total Prandtl number as a function of pressure and temperature. The expressions which comprise the curve fits give valid values when the input temperatures are between 500 and 30,000 K and the corresponding input pressures are between 1.0×10^{1} and 1.0×10^{7} N/m^2. For temperatures below 500 K, correlations valid for a perfect gas are employed.

Boundary Conditions

The viscous boundary conditions for perfect-gas and equilibrium airflow are identical. Their implementation, with the exception of the wall boundary condition, is also equivalent. The specification and implementation of the boundary conditions for viscous flow, except for the equilibrium wall condition, which is described below, can be found in Ref. 3.

As with perfect-gas flow, the wall boundary condition for equilibrium flow consists of a no-slip condition, a specified wall temperature, and a zero pressure gradient normal to the wall. The constraints on wall pressure and temperature are satisfied through an iterative procedure. Since Srinivasan et al.'s thermodynamic curve fits give temperature as a function of pressure and density, the pressure at the cell center adjacent to the wall is input and iterations on density are performed until the output temperature matches the specified wall temperature.

Results and Discussion

Surface pressure and heating predictions from LAURA are compared with corresponding predictions from a viscous shock layer (VSL) solver, and, in one case, with surface heating data obtained from a flight experiment. The freestream conditions for these cases are presented in Table 1.

For all cases presented, the error that is represented by the right-hand side of the governing equations is measured by an L_2 norm and solutions are considered converged when this value is below 10^{-5}. Also, to aid in the accurate prediction of the heat transfer, all of the grids used in this study have a cell Reynolds number at the wall that is approximately equal to one.

The additional work required for equilibrium computations results in an increase in CPU time when compared with the perfect-gas CPU time for the same problem. The reason for the increase is the inability of the curve fits used to take advantage of vector architecture and the additional time required by the iterative scheme to satisfy the wall boundary condition. On average, equilibrium computations increase the perfect-gas time per iteration per cell by 10%. This small increase is achieved by making periodic calls to the thermodynamic and transport property curve fits. Calls are made every 20 iterations rather than every iteration. The LAURA solutions presented in this article were computed using a single processor on a Cray Y-MP. The performance of the equilibrium algorithm was 35 μs/iteration/cell. This time is based on updating the left-hand side of the governing equations every iteration. Also, this time is representative for the cases presented in this article, because, in general, performance is dependent on the vector length, which is a function of grid size.

Case I

The first case presented is the Re-entry F vehicle. Re-entry F was a flight experiment conducted in the 1970s to extend turbulent heat-transfer data to conditions of high local Reynolds and Mach numbers, and to provide experimental data on boundary-layer transition during re-entry.[10] The Re-entry F

Table 1 Freestream conditions

Case	p_∞, N/m^2	T_∞, K	M_∞	Altitude, km	Re, m^{-1}
I	468.3	243.0	19.2	36	2.6×10^6
II	54.7	270.0	25.0	60	3.4×10^5
III	5.5	219.0	40.0	70	7.3×10^4

vehicle is a 5-deg sphere-cone with a 0.0029-m nose radius. LAURA solutions for a Mach 19 flow at 36-km altitude are computed over the vehicle for a length of 650 nose radii and are compared with a VSL solution and flight data. The grid consisted of 150 points in the streamwise direction and 81 points between the body and the outer boundary. The freestream conditions for the case are listed in Table 1. The wall temperature varies spatially from 4250 K at the stagnation point to 350 K at the outflow boundary, but is held constant in time.[18] Starting from freestream conditions, solutions were obtained in approximately 30 min of CPU time on a Cray Y-MP.

Figure 1 is a plot of the surface pressure distribution from LAURA and from the VSL.[18] Results are plotted as pressure nondimensionalized by the freestream density and velocity squared vs S/Rn. Over the length of cone considered, the agreement between LAURA and the VSL is very good. In the stagnation region, the two solution techniques predict values that are within 1% of each other. Along the first 20 nose radii, the flow expands rapidly with the pressure decreasing two orders of magnitude. The flow continues to expand before recompressing to the sharp-cone value. The values for the sharp-cone pressure predicted by the two techniques differ by 3%. Smaller differences are found in the overexpansion recompression region.

Predicted surface heating distributions are plotted in Fig. 2. Shown are predictions from LAURA and the VSL.[18] In addition, the heating distribution from the Re-entry F flight experiment is also shown. In the stagnation region, the agreement between LAURA and the VSL is within 5%. As the stagnation point is approached ($S/Rn < 0.5$), the two solutions begin to show differences larger than 5%. At the stagnation point this difference has grown to 10%. Along the cone flank the agreement between predicted heating values for the two computational techniques is very good. In this area, differences of 2% are noted. The agreement between LAURA and the flight data values for surface heating is comparable to the agreement noted between the VSL and the flight data. Both LAURA and the VSL underpredict the flight values by 8% at S/Rn equal to 250. For LAURA, this 8% difference decreases until it is 4% at the tail of the vehicle.

Difficulties in predicting values based on gradients near a grid singularity are not unique to LAURA, and surface heating in particular has been discussed by Grasso and Gnoffo[19] and Blottner.[20] According to Ref. 19, the cause of the difficulty is a truncation error that changes from second- to first-order at grid singularities (cells with a face area equal to 0 or infinite grid Jacobian). Such pie-shaped cells are present along the computational boundary between the geometric stagnation point and the freestream. Blottner overcame the problem by casting the offending term in nonconservation form. Gnoffo et al.[2] had moderate success at minimizing the influence of the grid singularity on gradient-sensitive quantities for blunt-body flows by using a volume-weighted flux. Grasso and Gnoffo[19] also found that increasing the grid resolution normal to the body had a positive affect. For slender bodies, smooth streamwise heating distributions can be obtained if points are suitably spaced near the stagnation point. For case I, points on the spherical nose were spaced at $\Delta S/Rn$ equal to 0.07. This spacing produced smooth heating distributions and provided an adequate number of points to resolve the rapidly expanding flow over the nose. It is emphasized that this spacing specification does not solve the problem, but serves only to help smooth heating distributions. Moreover, this specification is flow and geometry dependent.

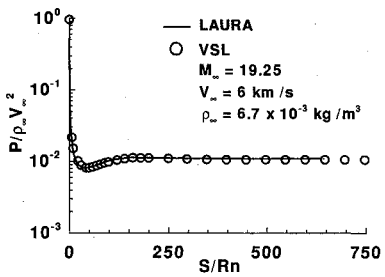

Fig. 1 Re-entry F surface pressure at 36-km altitude.

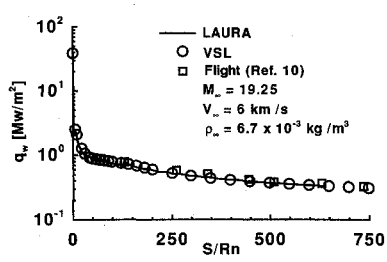

Fig. 2 Re-entry F surface heating rate distribution at 36-km altitude.

Table 2 Grid dimensions for case II

Grid	Points			Length,
	Streamwise	On nose	Normal	S/Rn
A	150	25	65	100
B	100	10	65	100

Case II

The second case presented is the Mach 25 flow over a 5-deg sphere-cone with a 0.038-m nose radius at an altitude of 60 km. The freestream conditions are given in Table 1. The wall temperature is 1255 K. LAURA predictions for surface heating and pressure are compared with a solution from a VSL code.[18] LAURA grid dimensions are listed in Table 2. Approximately 2.2 million words of computer memory and 30 min of computer time were required to converge a solution for the largest grid listed in Table 2.

The surface pressure along the symmetry plane is plotted in Fig. 3. Two LAURA solutions, obtained on grids which differed in streamwise resolution, are presented. The solution on grid B (100×65) was computed to resolve a stagnation heating problem and is included here for additional comparison. The heating results will be discussed in the following paragraph. Figure 3a is a plot of the pressure distribution over a cone length of 100 nose radii. In the figure, away from the stagnation region differences between the LAURA solutions are negligible, regardless of the differences in streamwise resolution on the nose. Overall, the comparison between LAURA and the VSL results is good. On the aft end of the cone ($S/Rn > 50.0$), LAURA and the VSL agree within 4%. Larger differences (6%) are found near the minimum in pressure associated with the overexpansion recompression region. Because of the differing amount of resolution in the stagnation region, the two LAURA solutions differ by 2–5% (see Fig. 3b) with the grid A (150×65) solution in slightly better agreement with the VSL data. At the stagnation point LAURA is in excellent agreement with the VSL.

Surface heating distributions from LAURA and the VSL are plotted in Fig. 4. Figure 4a indicates the agreement in heating between LAURA and the VSL is within 5%, and the differences between the two LAURA predictions for heating are negligible. The aforementioned agreement between LAURA and the VSL continues until very near the stagnation point ($S/Rn < 0.35$). Figure 4b is a plot of the heating in the stagnation region. Near the stagnation point, the heating distribution computed on grid A (150×65) is not smooth. This is due to the grid singularity problem. To smooth the heating distribution, the streamwise spacing on the nose was increased from $\Delta S/Rn$ equal 0.07 to 0.17. The result is plotted as the dashed line in Fig. 4b. As shown, increasing the spacing

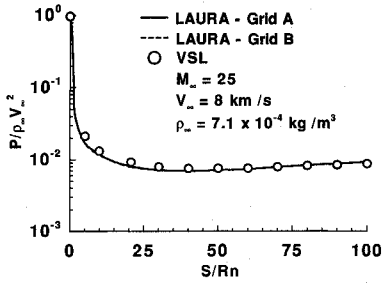

Fig. 3a Surface pressure distribution on a 5-deg cone at 60-km altitude.

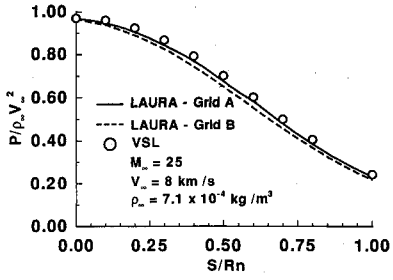

Fig. 3b Surface pressure distribution on a 5-deg cone at 60-km altitude (stagnation region).

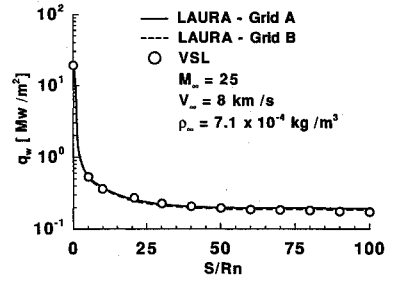

Fig. 4a Surface heating rate distribution on a 5-deg cone at 60-km altitude.

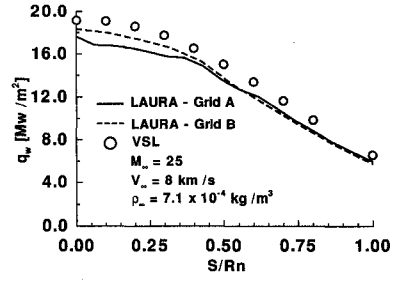

Fig. 4b Surface heating rate distribution on a 5-deg cone at 60-km altitude (stagnation region).

lessens the influence of the singularity on the heating. Agreement between the heating distributions from grids A (150×65) and B (100×65) is altered only very near the stagnation point. At the stagnation point a 3% difference is noted between LAURA (grid A) and the VSL. No attempt was made to determine the value of $\Delta S/Rn$ which would provide adequate resolution in the stagnation region and a smooth heating distribution.

Case III

The geometry used for the third case is shown in Fig. 5. It is a 60-deg sphere-cone with a circular aft shoulder. The nose radius is 3.23 m. The freestream conditions, which are in the range of consideration for Earth re-entry from Mars, are listed in Table 1. The wall temperature is a constant 1500 K. The grid consisted of 31 points in the streamwise direction and 129 points between the body and outer boundary. For this geometry, comparisons are made between LAURA and the VSL[18] predictions, with the results presented in Figs. 6 and 7. The VSL solution was computed over a cone without the circular aft shoulder, and as a result the VSL predictions do not reflect its influence. LAURA solutions required approximately 30 min of Cray YM-P time to converge from freestream conditions.

The surface pressure is plotted in Fig. 6. Overall, LAURA agrees well with the VSL. LAURA slightly underpredicts the pressure on the nose by 5%, but recovers, and is in good agreement on the cone flank. The rapid expansion noted in the LAURA solutions at S/Rn equal to 2.0 is due to the flow over the shoulder.

Heating rate predictions from LAURA and the VSL are plotted in Fig. 7. For grid A, LAURA agrees with the VSL for the stagnation value. Moving away from the stagnation point, percentage differences between the LAURA heating values for grid A and the VSL values remain constant until S/Rn equals 1.0. After this point, the differences between LAURA and the other heating rate predictions grow to 20%. The cell Reynolds number criterion mentioned earlier, and a grid spacing growth factor less than 1.2, have been adequate in the past for defining a grid upon which accurate heating results can be obtained, but appear not to apply to case III. For grid A, the maximum spacing growth in the normal direction is 1.15. Although this is on the high side of acceptable, past computations have not exhibited the behavior evidenced by grid A in Fig. 7.

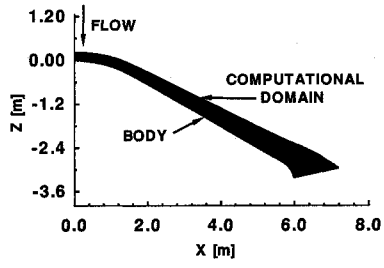

Fig. 5 Geometry for case III.

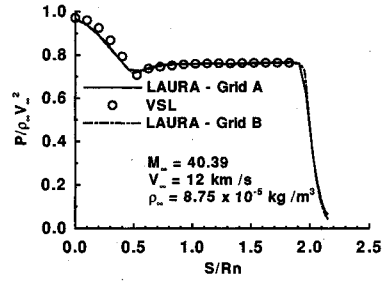

Fig. 6 Surface pressure distribution on a 60-deg cone at 70-km altitude.

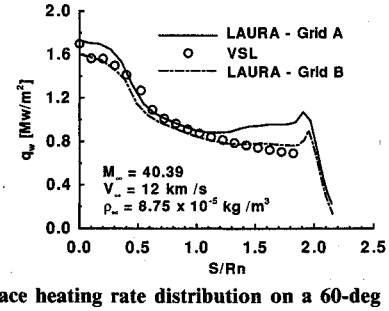

Fig. 7 Surface heating rate distribution on a 60-deg cone at 70-km altitude.

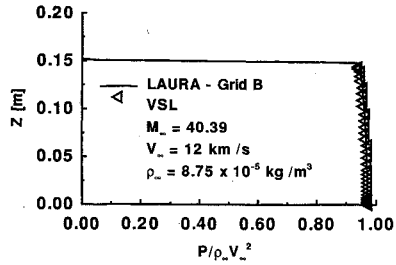

Fig. 8 Stagnation line pressure distribution.

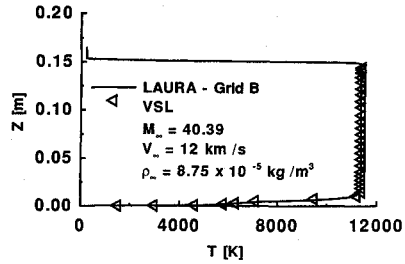

Fig. 9 Stagnation line temperature distribution.

To overcome the discrepancy in heating noted between the LAURA solution on grid A and the VSL, the grid stretching factor was reduced to 1.11. This change increased the resolution in the boundary layer on the cone flank. The LAURA solution using a factor of 1.11 is shown as grid B on Fig. 7. As indicated in the figure, the deviation between LAURA and the VSL is removed. At the stagnation point LAURA is within 8% of the VSL value, and over the nose and flank LAURA and the VSL heating rates are within 5%.

Profiles of pressure and temperature along the stagnation line are plotted in Figs. 8 and 9. LAURA agrees well with the VSL for both pressure and temperature, not only through the layer, but at the shock as well. These figures also show good agreement for the shock standoff distance. The LAURA solution captures the shock within 2 or 3 grid cells, whereas the VSL solution ends at the shock because it is a shock fitting scheme.

Concluding Remarks

This investigation details the modifications made to the LAURA algorithm that enable viscous equilibrium computations to be performed. The equilibrium option increases the computational cost by only a small percentage when compared with the cost of the perfect-gas algorithm. Although grid singularities appear not to affect the surface pressure, difficulties in obtaining smooth heating distributions in their vicinity have been noted and overcome by increasing the streamwise grid spacing near the singular point. Although increasing the spacing is not a solution of the problem and its specification is not straightforward, but rather a function of geometry and flow conditions, the relief it does provides does not affect the heating except in the immediate region of the singularity. The code has successfully computed the Mach 19 and Mach 25 flow over a 5-deg cone, and the Mach 40 flow over a 60-deg cone. The results of these computations are in excellent agreement with predictions from a VSL solver and in one case, with flight data.

References

[1]Gnoffo, P. A., "Application of Program LAURA to Three-Dimensional AOTV Flowfields," AIAA Paper 86-0565, Jan. 1986.

[2]Gnoffo, P. A., McCandless, R. N., and Yee, H. C., "Enhancements to Program LAURA for Computation of Three-Dimensional Hypersonic Flow," AIAA Paper 87-0280, Jan. 1987.

[3]Gnoffo, P. A., "An Upwind-Biased Point-Implicit Relaxation Algorithm for Viscous, Compressible Perfect-Gas Flows," NASA TP-2953, Feb. 1990.

[4]Gnoffo, P. A., Gupta , R. N., and Shinn, J. L., "Conservation Equations and Physical Models for Hypersonic Air Flows in Thermal and Chemical Nonequilibrium," NASA TP-2867, Feb. 1989.

[5]Thompson, R. A., and Gnoffo, P. A., "Application of the LAURA Code for Slender-Vehicle Aerothermodynamics," AIAA Paper 90-1714, June 1990.

[6]Weilmuenster, K. J., Smith, R. A., and Greene, F. A., "Assured Crew Return Vehicle Flowfield and Aerodynamic Characteristics," AIAA Paper 90-0229, Jan. 1990.

[7]Greene, F. A., Weilmuenster, K. J., and Micol, J. R., "Predicted Aerodynamics for a Proposed Personnel Launch Vehicle," AIAA Paper 90-1668, June 1990.

[8]Mitcheltree, R. A., and Gnoffo, P. A., "Thermochemical Nonequilibrium Issues for Earth Re-entry of Mars Mission Vehicles," AIAA Paper 90-1698, June 1990.

[9]Gupta, R. N., Lee, K. P., Zoby, E. V., Moss, J. N., and Thompson, R. A., "Hypersonic Viscous Shock-Layer Solutions over Long Slender Bodies—Part I: High Reynolds Number Flows," *Journal of Spacecraft and Rockets,* Vol. 27, No. 2, 1990, pp. 175–184.

[10]Stainback, P. C., Johnson, C. B., Boney, L. B., and Wicker, K. C., "Comparison of Theoretical Predictions and Heat Transfer Measurements for a Flight Experiment at Mach 20 (Re-entry F)," NASA TM X-2560, June 1972.

[11]Roe, P. L., "Approximate Riemann Solvers, Parameter Vectors and Difference Schemes," *Journal of Computational Physics,* Vol. 43, No. 2, 1981, pp. 357–372.

[12]Yee, H. C., "On Symmetric and Upwind TVD Schemes," NASA TM 86842, Sept. 1985.

[13]Grossman, B., and Walters, R. W., "Flux-Split Algorithms for the Multi-Dimensional Euler Equations with Real Gases," *Computers and Fluids,* Vol. 17, No. 1, 1989, pp. 99–112.

[14]Colella, P., and Glaz, P. M., "Efficient Solution Algorithms for the Riemann Problem for Real Gases," *Journal of Computational Physics,* Vol. 59, No. 2, 1985, pp. 264–289.

[15]Gupta, R. N., Lee, K. P., Thompson, R. A., and Yos, J. M., "Calculations and Curve Fits of Thermodynamic and Transport Properties for Equilibrium Air to 30000 K," NASA RP-1260, Oct. 1991.

[16]Anderson, J. D., Jr., *Hypersonic and High Temperature Gas Dynamics,* McGraw-Hill, New York, 1989.

[17]Srinivasan, S., Tannehill, J. C., and Weilmuenster, K. J., "Simplified Curve Fits for the Thermodynamic Properties of Equilibrium Air," NASA RP-1181, Aug. 1987.

[18]Gupta, R. N., private communication, NASA Langley Research Center, Hampton, VA, Dec. 1989.

[19]Grasso, F., and Gnoffo, P. A., "A Numerical Study of Hypersonic, Stagnation Heat Transfer Predictions at a Coordinate Singularity," 8th GAMM Conf. on Numerical Methods in Fluids Mechanics, Sept. 1989, pp. 179–188.

[20]Blottner, F., "Verification of a Navier-Stokes Code for Solving the Hypersonic Blunt Body Problem," Fourth Symposium on Numerical and Physical Aspects of Aerodynamic Flows, Jan. 1989.

Ernest V. Zoby
Associate Editor